Reviews of Electromagnetics, Vol. IV, 2025
EuCAP 2025 Special Issue
DOI: 10.53792/RoE/2025/25003

Reviews of Electromagnetics
EuCAP 2025 Special Issue

Multi-RIS-assisted Railway Communications in Tunnel using CloudRT simulator

Aline Habib[1*], Ammar El Falou[2], Charlotte Langlais [1], Marion Berbineau [3]

Abstract
High data rates are increasingly required in railway communications to support services such as video streaming, passenger connectivity, real-time monitoring, and safety-critical applications. Although millimeter-wave (mmWave) frequencies meet these demands due to their large available bandwidth, their strong sensitivity to blockage significantly limits their coverage, particularly in confined environments such as tunnels, where tunnel walls, ceilings, and train carriages can obstruct signals. In this context, Reconfigurable Intelligent Surfaces (RIS) have emerged as a promising solution to overcome signal-blocking issues by enabling additional propagation paths. However, due to the high signal attenuation in tunnel environments, a single RIS is generally insufficient to ensure reliable communication throughout the tunnel. Consequently, multiple RISs must be deployed along the tunnel to maintain an acceptable received signal. This paper investigates the effectiveness of multi-RIS-assisted systems in tunnel scenarios. An optimization algorithm is proposed to determine the optimal number and placement of RISs within the tunnel. A ray-tracing simulator, CloudRT, is used to generate realistic channel coefficients. As RIS functionality is not integrated into the simulator, we extend it by modeling the RIS as a virtual receiver-transmitter phased array antenna. The simulation results show that in tunnel scenarios where the direct Tx–Rx link is blocked by a train, placing the RIS on the tunnel's ceiling yields better performance than mounting it on the tunnel's walls. Moreover, the Rx can achieve a good signal-to-noise ratio (SNR) using a reasonable number of RISs of practical size.

Key terms
Railway communications; Reconfigurable intelligent surface; Tunnel environment; Ray tracer; RIS position

[1] *Mathematical and electrical engineering department, CNRS UMR 6285 Lab-STICC, IMT Atlantique, Brest, France*
[2] *CEMSE Division, King Abdullah University of Science and Technology (KAUST), Saudi Arabia*
[3] *COSYS-LEOST, Université Gustave Eiffel, Villeneuve d'Ascq, France*
[*] **Corresponding author**: Aline.Habib@imt-atlantique.fr

Received: 19/05/2025, Accepted: 06/07/2025, Published: 19/11/2025

1. Introduction

To meet the increasing demand for high data rates in railway communications for critical operations and Internet-based services, such as real-time video streaming and videoconferencing, millimeter wave technology (mmWave), ranging between 30 and 300 GHz, is emerging as a key solution [1, 2, 3]. However, mmWave communications face significant challenges due to the high penetration loss and sensitivity to obstructions [4]. Specifically, in confined railway environments, such as tunnels, signals can be blocked by tunnel walls, ceilings, and train carriages, resulting in a limited mmWave coverage area [5, 6]. In this context, reconfigurable intelligent surface (RIS) is a potential technology for solving mmWave blockage problems [7]. RIS is a planar structure composed of elements that reflects the incoming signals in a controlled manner by adjusting the phase shift [8, 9]. It can be passive or active according to its structure and function. Passive RIS operates without active RF components, minimizing power consumption [10], while active RIS uses amplifiers to enhance signals but consumes more power and generates more thermal noise [11]. To balance these trade-offs, [12] proposed a hybrid RIS, combining passive and active elements. In this paper, we consider a passive RIS, as it is more suitable for tunnel environments where power availability is limited and thermal management is challenging. Passive RIS enhances signal strength at the receiver (Rx) by creating additional propagation paths [13, 14]. It provides two links: one between the transmitter (Tx) and the RIS and another between the RIS and the Rx, effectively mitigating signal blockages and extending the coverage area [15]. In scattering-rich

environments, where signals encounter significant obstacles, the deployment of multiple RISs can effectively bypass signal obstructions between Tx and Rx, improving service coverage [16]. For instance, [17] solves the problem of dead zones in Rennes railway stations by deploying multiple RISs at optimal placements. Recently, RIS has been incorporated into various research fields, including vehicular communication [18, 19, 20], unmanned aerial vehicle communication (UAV) [21, 22, 23], underwater acoustic communication [24, 25, 26], and high-speed railway (HSR) networks [27, 28, 29, 30, 31], due to its ability to configure the environment [32], reduce interference [33], and mitigate Doppler shift [34]. [35] examined the primary challenges, key application scenarios, and a range of promising future directions for RIS in railway communications. In [36], the authors explored the optimal placement of RIS in high-speed train (HST) communications, showing that deployment on the train side effectively reduces delay spread and improves spectral efficiency. In [37], the authors proposed integrating RIS with the UAV to improve HSR communication when the direct link between the base station (BS) and the train is blocked and suggested optimization algorithms to maximize uplink cell capacity. The authors in [38] proposed a deep reinforcement learning (DRL)-based scheme to optimize RIS phase shifts, to mitigate interference in the HSR system. In [39] the authors investigated the use of RIS to improve safety in HSR networks where there is no direct link, demonstrating that the deployment of RIS with optimized phase shifts can significantly improve the performance of the integrated sensing and communication system, in terms of the sum rate. In [40], the authors proposed a scheduling approach for interrupt flows to enhance security capacity and then better meet the demand for passenger service in HSR networks assisted by RIS.

The previously mentioned papers focus on RIS-assisted HSR communications in outdoor environments, but the effectiveness of RIS in indoor tunnel environments remains underexplored. [41] evaluates the performance of a RIS-assisted communication system in a high-speed railway tunnel. It shows that RIS can extend tunnel coverage and that deploying multiple RIS or large RIS can significantly increase system capacity. However, the chosen channels are theoretical Rician channels, which do not realistically represent propagation in the tunnel. Moreover, tunnel environments present significant challenges to accurately measuring mmWave channels [42]. In this context, the ray tracer is a suitable choice, as it effectively models realistic geometries and generates reliable channel representations [43]. However, existing channel model simulators for RIS-assisted systems are not realistic in such an environment, and RIS is not an integrated device in a ray tracer simulator [44] where the applied reflection follows the Snell-Descartes law. In the literature, several approaches have been explored to integrate RIS into a ray tracer simulator, as in [45], a rotation of the normal of the Snell-Descartes law is applied in a ray tracer called Wireless Insite, modifying the traditional reflection to achieve directional reflection. In [46], RIS elements are represented as steerable interaction points, acting first as an Rx and then as a Tx where the expression of the electromagnetic field at the Rx is modified to account for the RIS phase shift. Also, in [47], the RIS is modeled as a virtual phased antenna array, operating first as an Rx and then as a Tx. In this paper, we integrate RIS into the CloudRT ray-tracing simulator, treating RIS as a virtual Rx antenna array and then as a virtual Tx antenna array. This study significantly extends our previous work presented in [48]. To the best of the authors' knowledge, it is the first to investigate the deployment of multiple RIS in a tunnel environment using a realistic raytracer channel simulator, CloudRT. The work evaluates the performance of a multi-RIS-assisted system in scenarios where the direct Tx–Rx link is blocked by a masking train and aims to determine the sufficient number of RIS units and their optimal location in the tunnel to achieve good performance.

The main contributions of this paper are summarized as follows.

- Integrate RIS into the CloudRT simulator to realistically study the propagation and behavior of RIS-assisted channels in a tunnel environment.
- Determine the optimal placement of the RIS in the tunnel among several candidate locations, such as the tunnel wall, the tunnel ceiling, and the top of the train.
- Formulate an optimization algorithm to determine the optimal number of RIS to deploy in the tunnel and their corresponding positions, ensuring that the signal-to-noise ratio (SNR) remains above a specified threshold for all train positions in the tunnel.

The remainder of this paper is organized as follows. Section 2 introduces the simulation environment, describes the CloudRT simulator, and details the integration of the RIS into this ray tracer simulator. The system model is defined in Section 3. Section 4 provides the numerical results. Finally, Section 5 concludes the paper.

2. Tunnel environment modeling and CloudRT simulator for RIS-assisted systems

2.1. Environment model

The ray-tracing simulations are performed in a double-track arched tunnel scenario. Due to infinite image generation, traditional ray-tracing models are unsuitable for curved surfaces. Faceting techniques address this issue by approximating curved surfaces with multiple flat facets [49]. The geometric model of the tunnel scene, designed using the 3D tool SketchUp, is illustrated in Fig. 1(a). It consists of 14 facets that form the arched section. The tunnel extends 100 meters along the x-axis, with a height of 5 meters along the z-axis and a width of 9 meters along the y-axis. Inside the tunnel, there is a moving train made of silver metal, measuring 20 meters in length and 3.94 meters in height. A stationary masking train obstructs the direct Tx-Rx path, and therefore, only the reflected rays, represented in blue in the scene as shown in Fig. 1(b), are obtained from the ray tracer simulation. The Tx, typically the BS, is placed at the tunnel entrance, while the Rx is mounted on the moving train, serving as a mobile relay (MR).

2.2. CloudRT simulator

The ray-tracing simulation is performed using CloudRT [50], a cloud-based, high-performance tool developed by Beijing

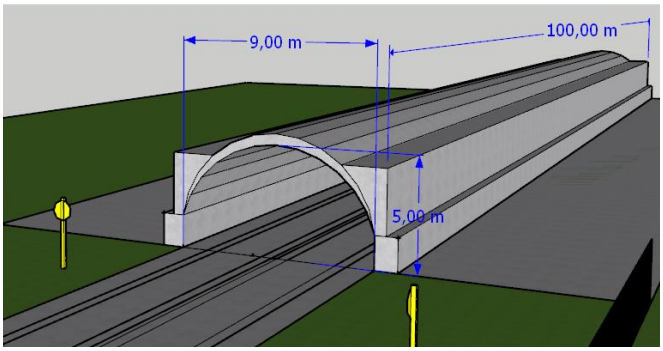

(a) Arched tunnel geometric model

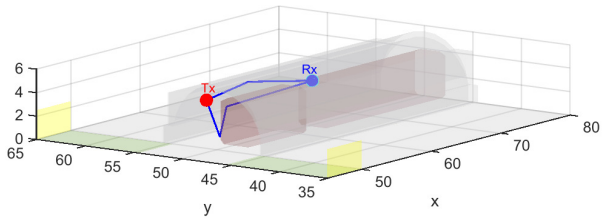

(b) Tunnel scene

Figure 1: Tunnel geometrical model.

Jiaotong University. It surpasses other ray-tracing simulators due to its high computational speed and the ability to model mobile scattering objects [51]. The platform includes three key libraries: The environment library, material library, and antenna library, each providing extensive resources to help users efficiently configure their simulations [52]. The CloudRT workflow is depicted in Fig. 2 [53]. The simulator requires the geometric model of the scene, the propagation rays to be considered in the simulations, such as direct, reflected, and scattered rays, the positions of Tx and Rx, and a frequency vector defined by [f_{start}, f_{step}, f_{end}]. CloudRT operates at frequencies ranging from 450 MHz to 325 GHz in static and dynamic environments. In dynamic environments, each Rx position is treated as a separate snapshot s in the CloudRT simulator with $s = 1, 2, \ldots, S$ and S denote the total number of snapshots. Specifically, the train's motion is modeled by running parallel simulations [54], each corresponding to a fixed Tx position and its associated Rx position. This results in a deterministic channel representation for each position of the train. For each simulation, 12 ray properties are obtained, including ray type, power gain, delay, departure and arrival azimuth and elevation angles, and scene intersection points for reflected rays [55], as illustrated in the red box in Fig.2. A precise analysis can be obtained using CloudRT since it can effectively reproduce multipath components (MPCs) in radio wave propagation, providing accurate and comprehensive multidimensional MPC information. In addition, the simulator calculates the channel transfer function, defined as follows:

$$H(f_n) = \sum_{k=1}^{K} G_{Tx} H_k(f_n) G_{Rx} \tag{1}$$

$$H_k(f_n) = \alpha_k(f_n) e^{j\phi_k(f_n)} \delta(\theta_{AoD} - \theta_{AoD,k}) \delta(\theta_{EoD} - \theta_{EoD,k}) \\ \delta(\theta_{AoA} - \theta_{AoA,k}) \delta(\theta_{EoA} - \theta_{EoA,k}) \tag{2}$$

where G_{Tx} and G_{Rx} represent the Tx and Rx antenna radiation pattern, $\alpha_k(f_n)$ and $\phi_k(f_n)$ represent the amplitude and the phase of ray k obtained by the simulation that run at frequency f_n as shown in Fig. 2. By applying the inverse fast Fourier transform (IFFT), the simulator then generates the channel impulse response as illustrated in Fig. 2.

2.3. Integration of RIS into CloudRT

In ray tracer simulations, RIS is treated as a virtual Rx/Tx antenna array. We model the M elements of RIS as M receiving points for the Tx-RIS channel and then as M transmitting points for the RIS-Rx channel. The complex-valued coefficient representing the link between Tx and the m-th RIS element, as well as between the m-th RIS element and Rx, are defined, respectively, as follows:

$$h_m = \sum_{k_1=1}^{K_1(m)} \breve{\alpha}_{k_1}(m) e^{j\breve{\varphi}_{k_1}(m)} \tag{3}$$

$$g_m = \sum_{k_2=1}^{K_2(m)} \tilde{\alpha}_{k_2}(m) e^{j\tilde{\varphi}_{k_2}(m)} \tag{4}$$

where $K_1(m)$ and $K_2(m)$ are the number of rays resulting from the m-th simulation for the Tx-RIS and RIS-Rx channels, respectively. $\breve{\varphi}_{k_1}(m)$ and $\breve{\alpha}_{k_1}(m)$ are the phase and amplitude of the k_1-th ray in the m-th Tx-RIS simulation, $\tilde{\varphi}_{k_2}(m)$ and $\tilde{\alpha}_{k_2}(m)$ are the phase and amplitude of the k_2-th ray in the m-th RIS-Rx simulation.

When the number of RIS elements is large, performing M simulations for the Tx–RIS and RIS–Rx links can be time-consuming. To address this issue, the authors in [56] propose simulating only the link between the first Tx and Rx antennas and applying the array steering vector to generate the MIMO channel coefficient matrix in a ray tracer simulator. Inspired by this approach, we first simulate a single link between the Tx and the first RIS element, seen as a reference element, and then apply the array steering vector at reception. Then we simulate a link between the first RIS element and the Rx and apply the array steering vector at transmission. A comparison between the simulation of all links and the application of the array steering vector confirms the validity of this simplified method. Therefore, the channel coefficients for the Tx-RIS and RIS-Rx links can be defined as follows:

$$\mathbf{H} = \sum_{k_1=1}^{K_1} \breve{\alpha}_{k_1} e^{j\breve{\varphi}_{k_1}} \mathbf{a}_{RIS}(\vec{\Theta}^a_{k_1}) \tag{5}$$

$$\mathbf{G} = \sum_{k_2=1}^{K_2} \tilde{\alpha}_{k_2} e^{j\tilde{\varphi}_{k_2}} \mathbf{a}_{RIS}(\vec{\Theta}^d_{k_2}) \tag{6}$$

$\mathbf{a}_{RIS}(\vec{\Theta}^a_{k_1})$ and $\mathbf{a}_{RIS}(\vec{\Theta}^d_{k_2})$ represent the array steering vectors at the RIS, corresponding to the angle of arrival (AoA) from Tx to RIS and the angle of departure (AoD) from the RIS to the Rx, respectively.

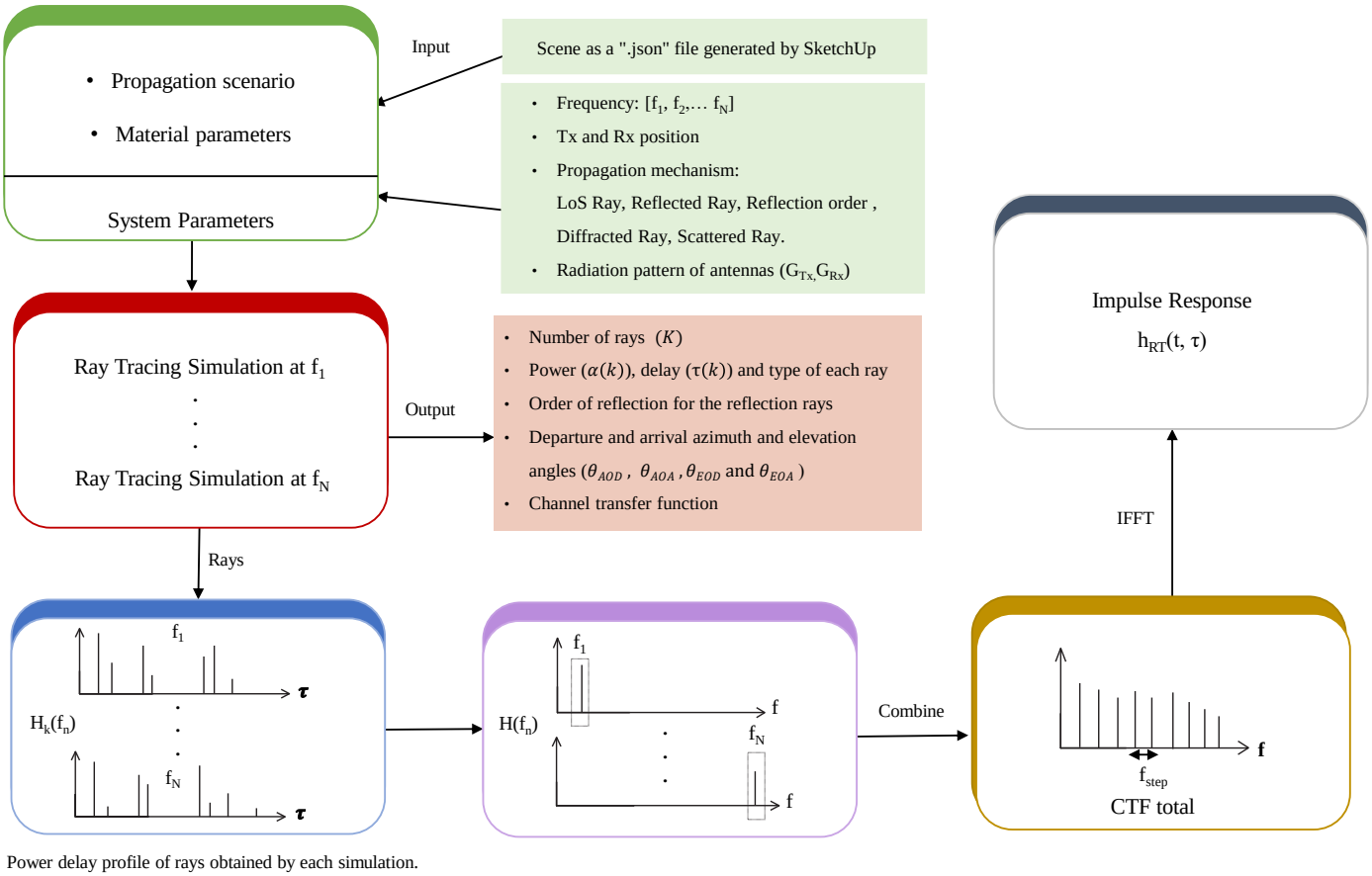

Figure 2: CloudRT simulator flow chart.

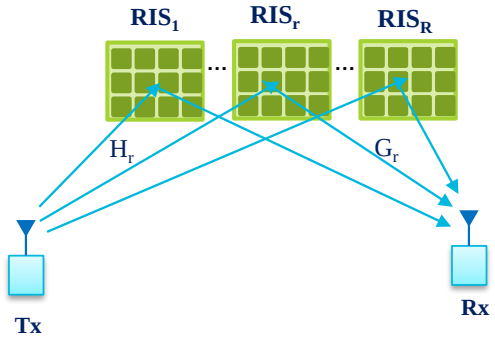

Figure 3: Multi-RIS assisted SISO system.

3. System model

The system investigated in this work is illustrated in Fig. 3. It consists of a single-input single-output (SISO) downlink narrowband system assisted by multi-RIS, where R RISs are deployed in the tunnel environment, each consisting of M elements. We assume that the R RISs operate independently, without cooperation between them [57]. Consequently, the phase shift of each element m of RIS r is defined similarly to that of a single RIS system with knowledge of the channel [6]. Additionally, we assume that the direct Tx-Rx channel is blocked, i.e., Rx only receives signal through the cascaded Tx-RIS-Rx channel. The signal received by the MR at each train position, s, can be defined as the superposition of all the signals arriving from the R Tx-RIS-Rx links [17], as follows

$$y(s) = \sqrt{P_t}\left(\sum_{r=1}^{R}\sum_{m=1}^{M} H_r(m)e^{j\theta_{r,s}(m)}G_{r,s}(m)\right)x + n(s) \qquad (7)$$

where $H_r(m)$ and $G_{r,s}(m)$ represent the complex coefficients of the channel between the m-th element of the r-th RIS and the Tx and Rx at a snapshot s, i.e., the MR position s, respectively. x is the transmitted signal, P_t the transmitted power, $n(s) \sim \mathcal{CN}(0, N_0)$ is the Rx noise, and $\theta_{r,s}(m)$ is the RIS phase shift of the m-th RIS element of the r-th RIS for the position s of the MR. Under the assumption of no cooperation between the R RISs, the phase shifts at each RIS can be optimized independently by maximizing the received power of the $Tx - RIS_r - Rx$ link. This leads to the following optimization problem for each RIS r:

$$\begin{aligned} \max_{\theta_{r,s}(m)} \quad & \left|\sum_{m=1}^{M} H_r(m)e^{j\theta_{r,s}(m)}G_{r,s}(m)\right|^2 \\ \text{s.t.} \quad & \theta_{r,s}(m) \in [0, 2\pi), \quad \forall r, m, s \end{aligned} \qquad (8)$$

The optimization problem defined by (8) is addressed R times, and the analytical solution of the optimal RIS phase shift for each RIS r in the case of a narrowband SISO system is then derived as shown in [27] by

$$\theta_{r,s}(m) = -\left(\arg(H_r(m)) + \arg(G_{r,s}(m))\right) \qquad (9)$$

where arg(.) represents the angle of a complex number, $H_r(m)$ and $G_{r,s}(m)$, respectively, denote the m-th element of the channel coefficient vectors $\mathbf{H}_r \in \mathbb{C}^{M\times 1}$ and $\mathbf{G}_{r,s} \in \mathbb{C}^{1\times M}$. These channel coefficient vectors can be defined as follows:

$$\mathbf{H}_r = \sum_{k_{1,r}=1}^{K_{1,r}} \breve{\alpha}_{k_{1,r}} e^{j\breve{\varphi}_{k_{1,r}}} \mathbf{a}_{RIS}(\vec{\Theta}^a_{k_{1,r}}) \tag{10}$$

$$\mathbf{G}_{r,s} = \sum_{k^s_{2,r}=1}^{K^s_{2,r}} \tilde{\alpha}_{k^s_{2,r}} e^{j\tilde{\varphi}_{k^s_{2,r}}} \mathbf{a}_{RIS}(\vec{\Theta}^d_{k^s_{2,r}}) \tag{11}$$

where $K_{1,r}$ and $K^s_{2,r}$ denote the number of paths between the Tx and the RIS r and the number of paths between the RIS r and the Rx at position s. $\breve{\alpha}_{k_{1,r}}$ and $\breve{\varphi}_{k_{1,r}}$ are the gain and the phase of the path $k_{1,r}$. $\tilde{\alpha}_{k^s_{2,r}}$ and $\tilde{\varphi}_{k^s_{2,r}}$ are the gain and the phase of the path $k^s_{2,r}$. $\mathbf{a}_{RIS}(\vec{\Theta}^a_{k_{1,r}})$ and $\mathbf{a}_{RIS}(\vec{\Theta}^d_{k^s_{2,r}})$ represent the array steering vectors at the RIS, corresponding to the AoA from Tx to RIS r and the AoD from the RIS r to the Rx at position s, respectively.

The array steering vector $\mathbf{a}(\vec{\tilde{\Theta}}_k)$ for the k^{th} path and a uniform rectangular antenna array positioned in the *xoy* plane, consisting of M_h horizontal antennas and M_v vertical antennas, which performs a directional transmission at an angle $\vec{\tilde{\Theta}}_k = (\tilde{\theta}_k, \tilde{\phi}_k)$, is defined as follows.

$$\mathbf{a}(\vec{\tilde{\Theta}}_k)) = \left[1, \cdots, e^{-j2\pi\frac{d}{\lambda}\left\{(M_h-1)\cos(\tilde{\theta}_k)\cos(\tilde{\phi}_k)+(M_v-1)\sin(\tilde{\phi}_k)\right\}}\right]^T \tag{12}$$

with $j \triangleq \sqrt{-1}$ the imaginary unit, λ the carrier wavelength and d the inter-element spacing distance.
Thus, the power received at each MR position s can be defined as

$$P_r(s) = 10\log_{10}\left|\sum_{r=1}^{R}\sum_{m=1}^{M} H_r(m) e^{j\theta_{r,s}(m)} G_{r,s}(m)\right|^2 P_t \tag{13}$$

4. Simulation results

Table 1: Simulation Parameters.

Parameter	Value
Frequency	30 [GHz]
Bandwidth	20 [MHz]
RIS elements separation distance	$\lambda/2$
Transmission power P_t	0 [dBm]
Antennas	Omnidirectional Vertical polarisation
Tx position	Tunnel entrance
Rx position	Top of the train
RIS position	Tunnel ceiling
Rays	Direct + reflection
Order of reflection	2

In this section, we first study the impact of the RIS phase shift on the received power and examine the optimal positioning of the RIS in the tunnel. Since the number of RISs does not affect the RIS phase shift or its positioning, we simplify the analysis by considering a system with a single RIS. The power received, defined in (13), is thus evaluated for $R = 1$. We then highlight the need for multiple RISs in the tunnel and determine the optimal number and placement of RIS. Unless stated otherwise, the simulation parameters are provided in Table 1.

4.1. Impact of RIS phase shift

To investigate the effect of RIS phase-shift optimization on received power, we plot in Fig. 4 the received power as a function of the number of RIS elements, M, for three values of RIS phase shift: i) optimal RIS phase shift, ii) suboptimal RIS phase shift, $\theta^{\text{subopt}}(m)$, and iii) random RIS phase shift, $\theta^{\text{rand}}(m)$. The optimal RIS phase shift is defined as in (9) for $r = 1$ and $s = 1$ for a single RIS and a fixed Rx. This RIS phase shift design requires full knowledge of the channel vectors $\mathbf{H}_r$ and $\mathbf{G}_{r,s}$. If only the LoS components of the channels are known, a suboptimal RIS phase shift can be applied using the LoS components only ($k_{1,r} = 1$ and $k^s_{2,r} = 1$) in $\mathbf{H}_r$ and $\mathbf{G}_{r,s}$. In this case, based on 9), the suboptimal RIS phase shift is given by:

$$\theta^{\text{subopt}}(m) = -\left(\arg(h_r(m)) + \arg(g_{r,s}(m))\right) \tag{14}$$

where $\mathbf{h}_r = \breve{\alpha}_1 e^{j\breve{\varphi}_1} \mathbf{a}_{RIS}(\vec{\Theta}^a_1)$ and $\mathbf{g}_{r,s} = \tilde{\alpha}^s_1 e^{j\tilde{\varphi}^s_1} \mathbf{a}_{RIS}(\vec{\Theta}^d_{1,s})$. The random RIS phase shifts follow a uniform distribution between 0 and 2π, given by

$$\theta^{\text{rand}}(m) \sim \mathscr{U}(0, 2\pi), \quad m = 1, 2, \ldots, M.$$

We can observe from Fig. 4 that the received power increases with M, as the increase in the number of RIS elements can compensate for the effect of double path loss resulting from cascaded channels. It is also clear that optimizing the RIS phase shift is necessary to achieve good performance. Although optimal phase shifts yield the highest received power, they require full channel state information (CSI), which can be challenging to acquire in practice, especially when the number of RIS elements is large. In contrast, suboptimal phase shifts depend only on LoS components, significantly reducing channel estimation overhead by requiring fewer estimated parameters. Therefore, a trade-off between performance and system complexity must be considered. In Section 4.3, we further investigate the impact of imperfect channel estimation on the achievable data rate by introducing an error model.

4.2. RIS position

To illustrate the impact of the positioning of RIS on the received power, we consider several RIS placements within an obstructed tunnel, as shown in Fig. 5. Specifically, the RIS is positioned on the tunnel wall, on the tunnel ceiling, and on the roof of the train.

Fig. 6 shows the resulting rays of the Tx-RIS-Rx channel for various RIS positions within the obstructed tunnel. To show the gain of the RIS when it is close to the Rx, we put the RIS on the roof of the train, assuming that in this case, the direct Tx-Rx link is not blocked[1]. In Fig. 7, we compare the power

[1] In the blocked tunnel, when the RIS is placed on the roof of the train, if the Tx-Rx link is blocked by a masking train, the Tx-RIS link will also be blocked.

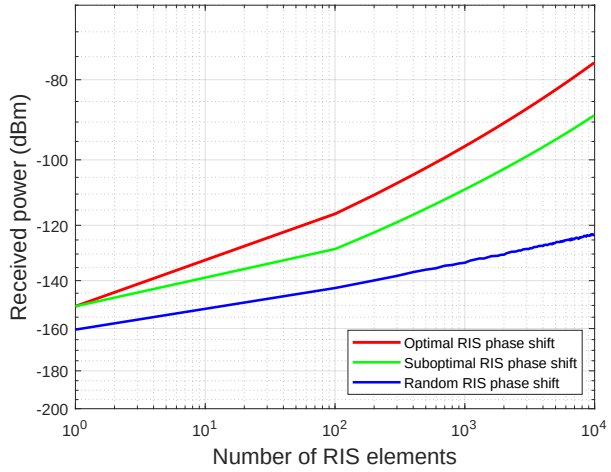

Figure 4: Received power versus the number of RIS elements for different RIS phase shift values.

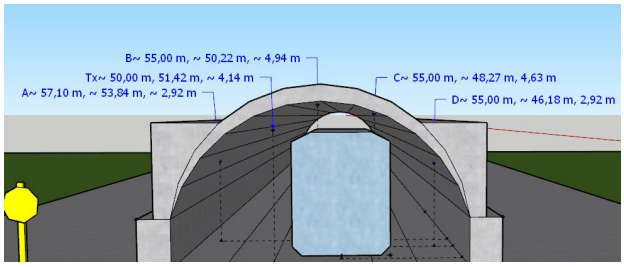

Figure 5: Illustration of the possible positions for RIS in a tunnel.

received by the MR as the train moves, considering different RIS positions: on the tunnel wall at positions A and D and on the tunnel ceiling at positions B and C to choose the appropriate placement of the RIS for this scenario. The received power decreases with the train's motion inside the tunnel as the path loss increases. Moreover, we can observe that it is advantageous to place the RIS on the ceiling of the tunnel at position B, where there is a masking train between Tx and Rx, and to avoid the deployment of the RIS on the wall of the tunnel at position D. Position D is not a good placement for the RIS since the train blocks the direct path between the Tx and the RIS, as shown in Fig. 6(d). When the RIS is placed on the roof of the train, close to Rx, we obtain the highest value of the received power.
We considered a tunnel scenario, where a masking train obstructs the direct path between Tx and Rx, to reflect a realistic case where an RIS can offer significant gains. However, even without the blocking train, extensive simulations for the same RIS positions show that placing the RIS on the train consistently yields the highest received power, with position B being the second best.

4.3. Channel estimation with errors

In this section, we study the system's robustness to channel imperfection by applying a model that consists of adding an error to the real **H** and **G** channel coefficients [58], This error model is represented by

$$\hat{\mathbf{H}} = \mathbf{H} + e_H \tag{15}$$

where e_H represents the estimation error following a normal distribution $\sim \mathscr{CN}(0, \sigma^2_{e_H})$ with variance $\sigma^2_{e_H} \triangleq \delta|\hat{\mathbf{H}}|^2$ while δ is the CSI error parameter. Assuming that the error is due to the train's movement, it will likely occur only on channel **G**, since the channel Tx-RIS is fixed. For comparison purposes, we also considered the case where **H** and **G** are erroneous. Fig. 8 shows the data rate, defined by (16), obtained under imperfect channel conditions for **G** or **H** and **G**, as a function of δ.

$$R = \begin{cases} \log_2\left(1 + \dfrac{\left|\sum_{m=1}^{M} H(m) e^{j\hat{\theta}(m)} \hat{G}(m)\right|^2 P_t}{P_N}\right), & \mathbf{G} \text{ with error,} \\ \log_2\left(1 + \dfrac{\left|\sum_{m=1}^{M} \hat{H}(m) e^{j\hat{\theta}(m)} \hat{G}(m)\right|^2 P_t}{P_N}\right), & \mathbf{G} \text{ and } \mathbf{H} \text{ with error} \end{cases} \tag{16}$$

where

$$\hat{\theta}(m) = \begin{cases} -(\arg(H(m)) + \arg(\hat{G}(m))), & \mathbf{G} \text{ with error,} \\ -(\arg(\hat{H}(m)) + \arg(\hat{G}(m))), & \mathbf{G} \text{ and } \mathbf{H} \text{ with error} \end{cases} \tag{17}$$

It is observed from this figure that the performance loss increases as δ increases. Comparing the imperfect case, where errors are added to both **H** and **G**, with the perfect case shows a loss of performance 7% when $\delta = 0.3$ and a loss 24% when $\delta = 0.6$, indicating that the system is relatively robust to errors. Moreover, the performance degradation is lower when only **G** is imperfect. These results are consistent with [59], where similar findings show that performance degradation becomes more significant as the number of erroneous channels increases. In the following section, we assume a perfect channel model.

4.4. Single to Multi-RIS assisted systems

To highlight the need for a multi-RIS-assisted system in a tunnel environment, we illustrate in Fig. 9 a heat map of the power values received by the MR, placed on the roof train, as the train moves through the tunnel. This figure compares a system assisted by a single RIS placed at the tunnel ceiling, the best position as determined in the previous section, with a system assisted by four RISs, also placed at the tunnel ceiling and distributed along the tunnel at the x coordinates 70, 85, 105, and 130 m. When a single RIS is deployed, the power received increases as the train approaches the RIS. However, as the train moves away from the RIS, the received power decreases considerably, showing that a single RIS is insufficient for long tunnels. With four RISs, the received power is improved even when the Rx reaches the end of the tunnel. Therefore, a multi-RIS approach is required to guarantee an acceptable received power signal along the tunnel.

Fig. 10 shows the received power as a function of the MR's position, x, for two RIS element sizes[2]: $M = 1{,}000$ and $M = 10{,}000$, with four RISs deployed in the tunnel. As the train

[2] A passive RIS provides negligible gain with a small number of RIS elements [11]. However, given the constraints of tunnel size, a trade-off must be made

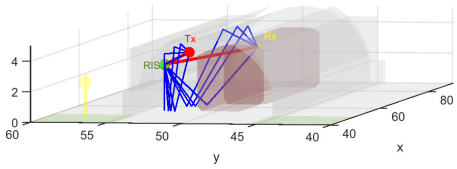

(a) RIS on the tunnel wall A

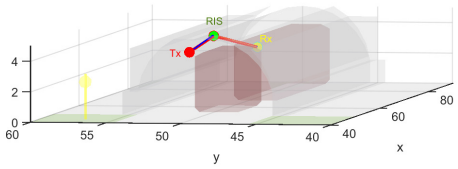

(b) RIS on the tunnel ceiling B

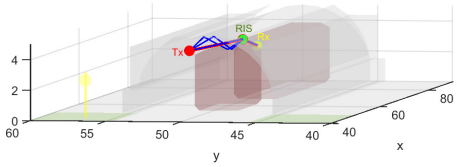

(c) RIS on the tunnel ceiling C

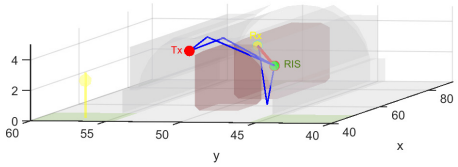

(d) RIS on the tunnel wall D

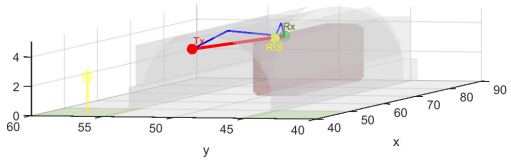

(e) RIS at the roof of the train without a masking train

Figure 6: Illustration of the resulting rays corresponding to the tunnel scene with a masking train for different RIS positions.

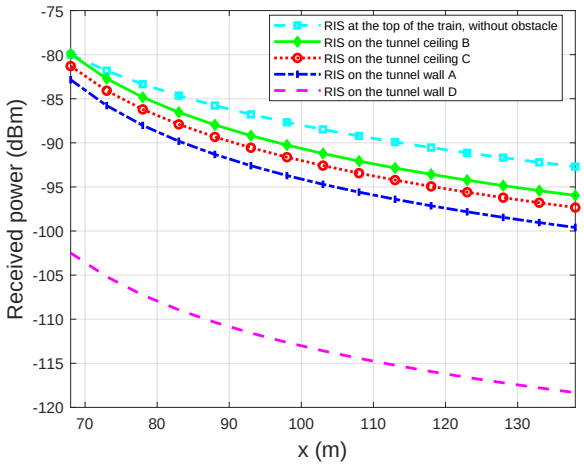

Figure 7: Received power by the MR versus the Tx-Rx separation distance for different positions of RIS.

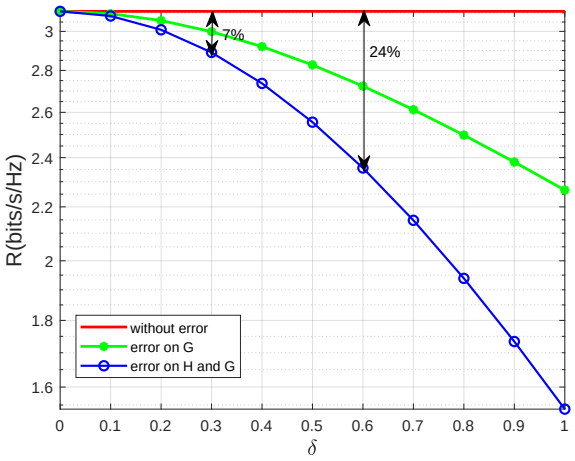

Figure 8: Data rate as a function of the error parameter δ, considering errors on channel coefficients G and/or H, and ideal case without error.

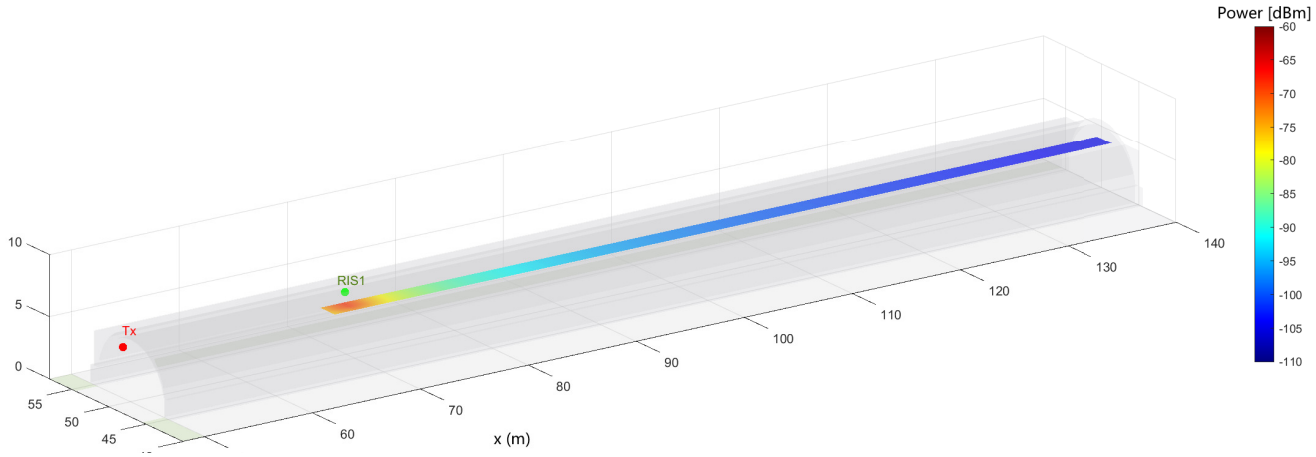

(a) Heat map with 1 RIS

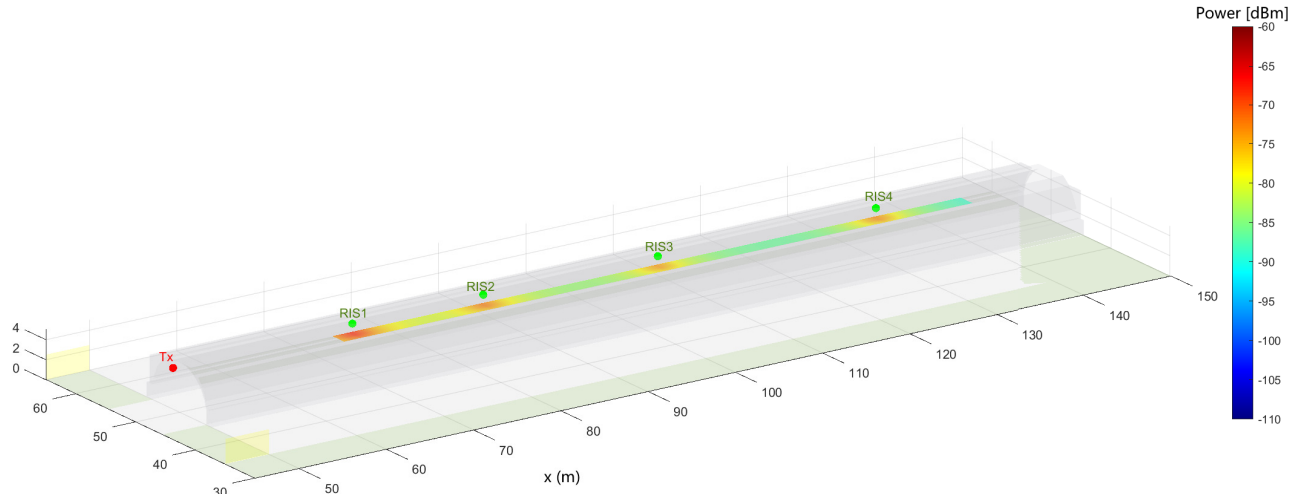

(b) Heat map with 4 RISs

Figure 9: Heat map showing the received power at the mobile relay located on the train roof, with one and for RISs deployed.

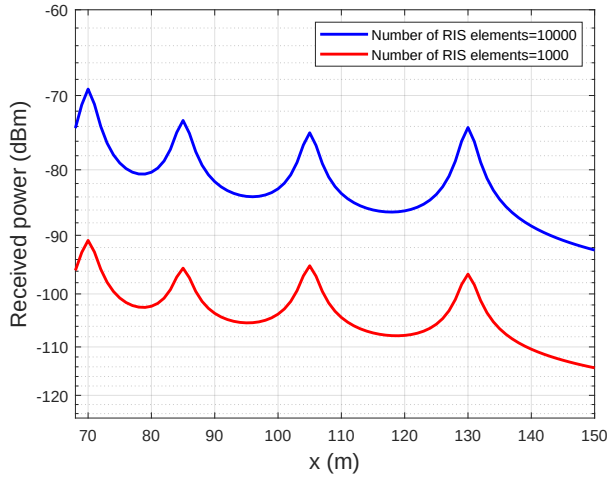

Figure 10: Received power at the MR as a function of train motion, x, for two numbers of RIS elements.

moves through the tunnel and moves away from Tx, the received power decreases due to path loss. Moreover, increasing the number of RIS elements enhances the received power, as more elements can better compensate for the effects of double-path loss. Additionally, four peaks in received power are observed, corresponding to the positions of the RIS. At these positions, the MR is closer to the RIS, allowing it to receive stronger reflected signals.

These results reflect the interest of multiple RISs in the tunnel. However, the number of RIS and their placement are currently arbitrary. In the following section, we apply an optimization algorithm to determine the optimal number and positioning of RIS in the tunnel.

4.5. Number of RIS

We apply a heuristic optimization algorithm to determine the required number of RIS and their position in the tunnel. The algorithm 1 starts by positioning two RISs, one at the entrance and the other in the middle of the tunnel. Then it calculates the signal-to-noise ratio (SNR) at each MR position, as $SNR(s) = \frac{P_r(s)}{P_N}$ and compares it with a predefined SNR threshold. This threshold is determined to ensure that train passengers can reliably use applications such as video conferencing, which require a spectral efficiency ν greater than 2 bits/s/Hz. If the SNR at any position is below the threshold, an additional RIS is placed at the position with the lowest SNR. This process is repeated until the SNR exceeds the threshold at all positions. Fig. 11 plots the SNR as a function of MR position for each iteration according to Algorithm 1. From this figure, we can conclude that eight RISs are sufficient to obtain an SNR higher than the SNR threshold for all MR positions.

between increasing the number of RIS elements and the maximum deployable size within the tunnel. According to [15], an RIS with 10,000 elements offers good performance, and the corresponding size is 50×50 cm^2. This confirms that the choice of $M = 10,000$ is practical and feasible within the constraints of the tunnel size.

Algorithm 1 Number of RIS and RIS position

Input: TxPosition, RxPosition, SNR_{th}, R_{max}
Output: R, RIS_positions

Initialize RIS_positions:

$$\text{RIS\_positions} \leftarrow \begin{bmatrix} xstart, 50.2, 4.94 \\ \frac{xstart+xend}{2}, 50.2, 4.94 \end{bmatrix}$$

$R \leftarrow 2$
for $r = 1$ to R **do**
  Run **simulation1TxRIS**(TxPosition, RIS_positions[r])
  Find channel coefficients H_r
  Run **simulation2RISRx**(RIS_positions[r], RxPosition)
  Find channel coefficients G_r
end for
Calculate SNR
while $R < R\_max$ **and any**($SNR < SNR_{th}$) **do**
  Find minimum SNR index min_index
  Add a RIS to $RIS\_positions$ with x=min_index
  $R \leftarrow R + 1$
  for $r = 1$ to R **do**
    Run**simulation1TxRIS**(TxPosition,RIS_positions[r])
    Find channel coefficients H_r
    Run **simulation2RISRx**(RIS_positions[r], RxPosition)
    Find channel coefficients G_r
  end for
  Recalculate SNR
end while

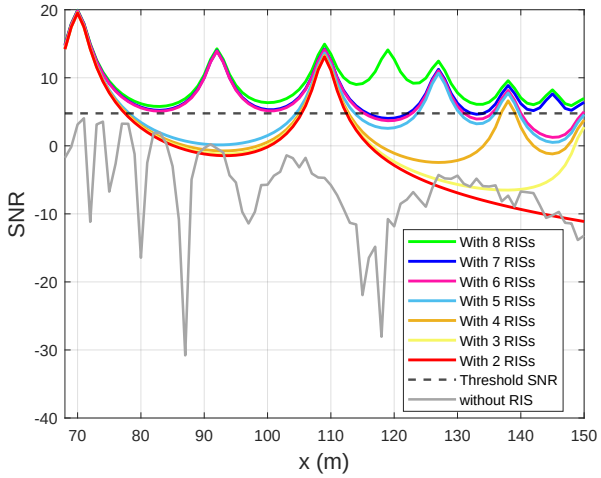

Figure 11: SNR as a function of train motion, x, with different numbers of RISs deployed and without RIS.

5. Conclusion

In this paper, we investigate a multi-RIS-assisted SISO system in an obstructed tunnel environment, using the CloudRT ray-tracing tool to model the channel propagation behavior realistically. We first integrated the RIS into the simulator by modeling it as a virtual Rx/Tx phased antenna array. We then compared the power received by the MR in a system assisted by a single RIS versus a system assisted by multiple RISs. The results highlight the necessity of deploying multiple RISs in tunnel environments, where the tunnel length makes a single RIS insufficient to maintain acceptable signal quality throughout the train's movement inside the tunnel. Therefore, we proposed an optimization algorithm to determine the required number and optimal position of RIS in the tunnel. Simulation results show that i) increasing the number of RIS elements significantly improves the received power, ii) optimal phase shift configuration at the RIS is critical for good system performance, iii) in the studied arched tunnel scenario, when the direct Tx-Rx link is blocked by a masking train, placing the RIS on the tunnel ceiling yields better performance than placing it on the tunnel wall or the train roof, and iv) the system shows relative robustness to CSI errors. Omnidirectional antennas were chosen in this study to maintain a generic propagation scenario and to highlight the contribution of the RIS to the system performance. In future work, we plan to incorporate directional antennas, which offer higher gain and are better suited to compensate for the significant path loss at mmWave frequencies. Additionally, the effectiveness of multiple RISs in other types of tunnel scenarios, such as curved tunnels and narrow single-track tunnels, which present a higher likelihood of signal blockage, is left for future work.

Acknowledgment

This work was funded by the Council of the Region Bretagne, under the grant MILLIRIS and the French ANR project mmW4Rail under the grant ANR-20-CE22-0011. As far as CloudRT is concerned, the authors would like to thank Prof. Ke Guan from Beijing Jiaotong University for providing access to the CloudRT simulator and Yiran Wang for her support and guidance.

References

[1] M. A. Kishk and M.-S. Alouini, "Exploiting randomly located blockages for large-scale deployment of intelligent surfaces," *IEEE Journal on Selected Areas in Communications*, vol. 39, no. 4, pp. 1043–1056, 2020.

[2] H. Yin, R. Jiang, and Y. Xu, "An mmwave-based adaptive multi-beamforming scheme for high speed railway communications," in *10th International Conference on Wireless Communications and Signal Processing (WCSP)*, 2018.

[3] B. Ai, A. F. Molisch, M. Rupp, and Z.-D. Zhong, "5G key technologies for smart railways," *Proceedings of the IEEE*, vol. 108, no. 6, pp. 856–893, 2020.

[4] Q. Tu, Z. Dong, X. Zou, and N. Wei, "Physical layer security enhancement for mmWave system with multiple RISs and imperfect CSI," *IEICE Transactions on Communications*, vol. 107, no. 6, pp. 430–445, 2024.

[5] F. Naaz, A. Nauman, T. Khurshaid, and S.-W. Kim, "Empowering the vehicular network with RIS technology: a state-of-the-art review," *Sensors*, vol. 24, no. 2, 2024.

[6] C. Chen and C. Pan, "Blocking probability in obstructed tunnels with reconfigurable intelligent surface," *IEEE Communications Letters*, vol. 26, no. 2, pp. 458–462, 2021.

[7] J. He, F. Jiang, K. Keykhosravi, J. Kokkoniemi, H. Wymeersch, and M. Juntti, "Beyond 5G RIS mmWave systems: Where communication and localization meet," *IEEE Access*, vol. 10, pp. 68 075–68 084, 2022.

[8] E. Basar, M. Di Renzo, J. De Rosny, M. Debbah, M.-S. Alouini, and R. Zhang, "Wireless communications through reconfigurable intelligent surfaces," *IEEE access*, vol. 7, pp. 116 753–116 773, 2019.

[9] X. Ma, Y. Fang, H. Zhang, S. Guo, and D. Yuan, "Cooperative beamforming design for multiple RIS-assisted communication systems," *IEEE Transactions on Wireless Communications*, vol. 21, no. 12, pp. 10 949–10 963, 2022.

[10] K. Zhi, C. Pan, H. Ren, K. K. Chai, and M. Elkashlan, "Active RIS versus passive RIS: Which is superior with the same power budget?" *IEEE Communications Letters*, vol. 26, no. 5, pp. 1150–1154, 2022.

[11] Z. Zhang, L. Dai, X. Chen, C. Liu, F. Yang, R. Schober, and H. V. Poor, "Active RIS vs. passive RIS: Which will prevail in 6G?" *IEEE Transactions on Communications*, vol. 71, no. 3, pp. 1707–1725, 2022.

[12] N. T. Nguyen, V.-D. Nguyen, Q. Wu, A. Tölli, S. Chatzinotas, and M. Juntti, "Hybrid active-passive reconfigurable intelligent surface-assisted multi-user MISO systems," in *23rd International Workshop on Signal Processing Advances in Wireless Communication (SPAWC)*, 2022.

[13] Y. Wang, Y. Zhang, Y. Ren, L. Pang, Y. Chen, and J. Li, "Joint BS-RIS-user association and deployment design for multi-RIS-aided wireless networks," *IEEE Communications Letters*, 2024.

[14] Y. Liu, X. Liu, X. Mu, T. Hou, J. Xu, M. Di Renzo, and N. Al-Dhahir, "Reconfigurable intelligent surfaces: Principles and opportunities," *IEEE communications surveys & tutorials*, vol. 23, no. 3, pp. 1546–1577, 2021.

[15] A. Habib, I. Khaled, A. El Falou, and C. Langlais, "Extended NYUSIM-based mmwave channel model and simulator for RIS-assisted systems," in *Joint European Conference on Networks and Communications & 6G Summit (EuCNC/6G Summit)*, 2023, pp. 198–203.

[16] C. Huang, Z. Yang, G. C. Alexandropoulos, K. Xiong, L. Wei, C. Yuen, Z. Zhang, and M. Debbah, "Multi-hop RIS-empowered terahertz communications: A DRL-based hybrid beamforming design," *IEEE Journal on Selected Areas in Communications*, vol. 39, no. 6, pp. 1663–1677, 2021.

[17] A. Albanese, G. Encinas-Lago, V. Sciancalepore, X. Costa-Pérez, D.-T. Phan-Huy, and S. Ros, "RIS-aware indoor network planning: The rennes railway station case," in *ICC International Conference on Communications*, 2022, pp. 2028–2034.

[18] Y. Chen, Y. Wang, J. Zhang, and M. Di Renzo, "QoS-driven spectrum sharing for reconfigurable intelligent surfaces (RISs) aided vehicular networks," *IEEE Transactions on Wireless Communications*, vol. 20, no. 9, pp. 5969–5985, 2021.

[19] M. Deng, M. Ahmed, A. Wahid, A. A. Soofi, W. U. Khan, F. Xu, M. Asif, and Z. Han, "Reconfigurable intelligent surfaces enabled vehicular communications: A comprehensive survey of recent advances and future challenges," *IEEE Transactions on Intelligent Vehicles*, 2024.

[20] M. Alsenwi, M. Abolhasan, and J. Lipman, "Intelligent and reliable millimeter wave communications for RIS-aided vehicular networks," *IEEE Transactions on Intelligent Transportation Systems*, vol. 23, no. 11, pp. 21 582–21 592, 2022.

[21] B. Xiong, Z. Zhang, C. Pan, and J. Wang, "Performance analysis of aerial RIS auxiliary mmWave mobile communications with UAV fluctuation," *IEEE Wireless Communications Letters*, vol. 13, no. 4, pp. 1183–1187, 2024.

[22] A. C. Pogaku, D.-T. Do, B. M. Lee, and N. D. Nguyen, "UAV-assisted RIS for future wireless communications: A survey on optimization and performance analysis," *IEEE Access*, vol. 10, pp. 16 320–16 336, 2022.

[23] L. Yang, F. Meng, J. Zhang, M. O. Hasna, and M. Di Renzo, "On the performance of RIS-assisted dual-hop UAV communication systems," *IEEE Transactions on Vehicular Technology*, vol. 69, no. 9, pp. 10 385–10 390, 2020.

[24] R. P. Naik and W.-Y. Chung, "Evaluation of reconfigurable intelligent surface-assisted underwater wireless optical communication system," *Journal of Lightwave Technology*, vol. 40, no. 13, pp. 4257–4267, 2022.

[25] Z. Sun, H. Guo, and I. F. Akyildiz, "High-data-rate long-range underwater communications via acoustic reconfigurable intelligent surfaces," *IEEE Communications Magazine*, vol. 60, no. 10, pp. 96–102, 2022.

[26] M.-H. T. Nguyen, E. Garcia-Palacios, T. Do-Duy, O. A. Dobre, and T. Q. Duong, "UAV-aided aerial reconfigurable intelligent surface communications with massive MIMO system," *IEEE Transactions on Cognitive Communications and Networking*, vol. 8, no. 4, pp. 1828–1838, 2022.

[27] A. Habib, A. E. Falou, C. Langlais, and M. Berbineau, "Reconfigurable intelligent surface assisted railway communications: A survey," in *97th Vehicular Technology Conference (VTC2023-Spring)*, 2023, pp. 1–5.

[28] J. Xu and B. Ai, "When mmwave high-speed railway networks meet reconfigurable intelligent surface: A deep reinforcement learning method," *IEEE Wireless Communications Letters*, vol. 11, no. 3, pp. 533–537, 2021.

[29] Y. Wang, G. Wang, R. He, B. Ai, and C. Tellambura, "Doppler shift and channel estimation for intelligent transparent surface assisted communication systems on high-speed railways," *IEEE Transactions on Communications*, vol. 71, no. 7, pp. 4204–4215, 2023.

[30] M. Gao, B. Ai, Y. Niu, Q. Li, Z. Han, Z. Zhong, X. Shen, and N. Wang, "IRS-assisted high-speed train communications: Performance analysis and optimal configuration," *IEEE Internet of Things Journal*, vol. 10, no. 21, pp. 18 980–18 992, 2023.

[31] J. Xu, C. Shan, L. Wu, Q. Zhang, S. Liu, and B. Ai, "Deep reinforcement learning for RIS-empowered high-speed railway cell-free networks," *IEEE Wireless Communications Letters*, vol. 12, no. 12, pp. 2078–2082, 2023.

[32] Y. Ma, K. Ota, and M. Dong, "Multi-RIS deployment location optimization for coverage enhancement in outdoor wireless communication networks," *IEEE Transactions on Vehicular Technology*, 2024.

[33] M. A. ElMossallamy, K. G. Seddik, W. Chen, L. Wang, G. Y. Li, and Z. Han, "RIS optimization on the complex circle manifold for interference mitigation in interference channels," *IEEE Transactions on Vehicular Technology*, vol. 70, no. 6, pp. 6184–6189, 2021.

[34] E. Basar, "Reconfigurable intelligent surfaces for doppler effect and multipath fading mitigation," *frontiers in Communications and Networks*, vol. 2, p. 672857, 2021.

[35] J. Zhang, H. Liu, Q. Wu, Y. Jin, Y. Chen, B. Ai, S. Jin, and T. J. Cui, "RIS-aided next-generation high-speed train communications: Challenges, solutions, and future directions," *IEEE Wireless Communications*, vol. 28, no. 6, pp. 145–151, 2021.

[36] K. Wang, C.-T. Lam, and B. K. Ng, "How to deploy RIS to minimize delay spread in HST communications: Railroad side, or train side?" in *22nd International Conference on Communication Technology (ICCT)*, 2022, pp. 793–797.

[37] Z. Liu, M. Yang, J. Cui, Y. Xiao, and X. Zhang, "Performance and capacity optimization for high speed railway communications using UAV-IRS assisted massive MIMO system," *Electronics*, vol. 12, no. 11, p. 2547, 2023.

[38] Z. Ma, Y. Wu, M. Xiao, G. Liu, and Z. Zhang, "Interference suppression for railway wireless communication systems: A reconfigurable intelligent surface approach," *IEEE Transactions on Vehicular Technology*, vol. 70, no. 11, pp. 11 593–11 603, 2021.

[39] P. Li, Y. Niu, H. Wu, Z. Han, G. Sun, N. Wang, Z. Zhong, and B. Ai, "RIS-assisted high-speed railway integrated sensing and communication system," *IEEE Transactions on Vehicular Technology*, vol. 72, no. 12, pp. 15 681–15 692, 2023.

[40] P. Li, Y. Niu, H. Wu, Z. Han, B. Ai, N. Wang, and Z. Zhong, "RIS-assisted scheduling for high-speed railway secure communications," *IEEE Transactions on Vehicular Technology*, vol. 72, no. 3, pp. 3488–3501, 2022.

[41] Y. Shao, H. Wang, D. Wang, T. Song, and J. Chen, "Channel modeling and performance analysis of RIS-assisted MIMO communications in high-speed rail tunnels," in *2023 9th International Conference on Computer and Communications (ICCC)*. IEEE, 2023, pp. 184–189.

[42] S. Li, Y. Liu, L. Lin, and Q. Sun, "Measurements and characterization for millimeter-wave massive MIMO channel in high-speed railway station environment at 28 GHz," *International Journal of Antennas and Propagation*, vol. 2021, no. 1, p. 4580506, 2021.

[43] K. Guan, D. He, B. Ai, D. W. Matolak, Q. Wang, Z. Zhong, and T. Kürner, "5-GHz obstructed vehicle-to-vehicle channel characterization for internet of intelligent vehicles," *IEEE Internet of Things Journal*, vol. 6, no. 1, pp. 100–110, 2018.

[44] Z. Li, O. A. Topal, Ö. T. Demir, E. Björnson, and C. Cavdar, "mmWave coverage extension using reconfigurable intelligent surfaces in indoor dense spaces," in *ICC International Conference on Communications*, 2023, pp. 5805–5810.

[45] J. Huang, C.-X. Wang, Y. Sun, J. Huang, and F.-C. Zheng, "A novel ray tracing based 6G RIS wireless channel model and RIS deployment studies in indoor scenarios," in *33rd Annual International Symposium on Personal, Indoor and Mobile Radio Communications (PIMRC)*, 2022, pp. 884–889.

[46] J. Pyhtilae, J. Kokkoniemi, P. Sangi, N. Vaara, and M. Juntti, "Ray tracing based radio channel modelling applied to RIS," in *WSA & SCC 2023; 26th International ITG Workshop on Smart Antennas and 13th Conference on Systems, Communications, and Coding*. VDE, 2023, pp. 1–6.

[47] J. Huang, C.-X. Wang, S. Yang, Y. Wang, Y. Xu, Y. Sun, J. Huang, and F.-C. Zheng, "Ray tracing based 6G RIS-assisted MIMO channel modeling and verification," in *International Conference on Communications in China (ICCC)*, 2023.

[48] A. Habib, C. Langlais, A. El Falou, S. Kangoute, Y. Wang, and M. Berbineau, "Integration of RIS into CloudRT simulator for railway tunnel scenarios," in *European Conference on Antennas and Propagation (EuCAP)*, 2025.

[49] E. Masson, "Etude de la propagation des ondes électromagnétiques dans les tunnels courbes de section non droite pour des applications métro et ferroviaire," Ph.D. dissertation, Université de Poitiers, 2010.

[50] Raytracer.cloud. (2025) Raytracer cloud. Accessed: 2025-04-07. [Online]. Available: http://www.raytracer.cloud

[51] L. Wang, K. Guan, B. Ai, G. Li, D. He, R. He, L. Tian, J. Dou, and Z. Zhong, "An accelerated algorithm for ray tracing simulation based on high-performance computation," in *11th International Symposium on Antennas, Propagation and EM Theory (ISAPE)*, 2016, pp. 512–515.

[52] K. Guan, H. Yi, D. He, B. Ai, and Z. Zhong, "Towards 6G: Paradigm of realistic terahertz channel modeling," *China Communications*, vol. 18, no. 5, pp. 1–18, 2021.

[53] J. Yang, B. Ai, I. You, M. Imran, L. Wang, K. Guan, D. He, Z. Zhong, and W. Keusgen, "Ultra-reliable communications for industrial internet of things: Design considerations and channel modeling," *IEEE Network*, vol. 33, no. 4, pp. 104–111, 2019.

[54] K. Guan, H. Yi, D. He, B. Ai, and Z. Zhong, "Towards 6G: Paradigm of realistic terahertz channel modeling," *China Communications*, vol. 18, no. 5, pp. 1–18, 2021.

[55] K. Guan, B. Ai, D. He, F. Zhu, H. Yi, J. Dou, and Z. Zhong, "Channel sounding and ray tracing for thz channel characterization," in *13th UK-Europe-China Workshop on Millimetre-Waves and Terahertz Technologies (UCMMT)*, 2020.

[56] J. Weng, X. Tu, Z. Lai, S. Salous, and J. Zhang, "Indoor massive MIMO channel modelling using ray-launching simulation," *International Journal of Antennas and Propagation*, vol. 2014, no. 1, p. 279380, 2014.

[57] D. Kong, S. Nambala, F. Rusek, and X. Cai, "Base-station and RIS deployment optimization for indoor coverage enhancement," in *Conference on Antenna Measurements and Applications (CAMA)*, 2023, pp. 246–249.

[58] Z. Zhang and L. Dai, "A joint precoding framework for wideband reconfigurable intelligent surface-aided cell-free network," *IEEE Transactions on Signal Processing*, vol. 69, pp. 4085–4101, 2021.

[59] K. M. Hamza, S. Basharat, S. A. Hassan, and H. Jung, "On the secrecy performance of RIS-enhanced aerial communication under imperfect CSI," in *INFOCOM 2023-IEEE Conference on Computer Communications Workshops (INFOCOM WKSHPS)*, 2023.